

Sustainable Solvent Recycling On-site with Automated Rotary Evaporation Systems

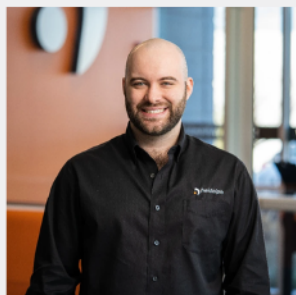
April 20, 10:00am - 11:00am EDT

With the steadily increasing costs of solvents and the huge CO₂ emissions associated with the production of new solvents, on-site solvent recycling is not only a suitable way to reduce operating costs in the lab but also a sensible step towards more sustainable processes. An example is the life cycle of acetone: the production of 1 ton of acetone causes about 2000 kg of CO₂ carbon footprint.

Watch this session during the WAS Virtual Conference:



Jürgen Heyder





Nate Kunzer



Lee Hibbett

[Register Now](#)

Comparing lipid remodeling of brown adipose tissue, white adipose tissue, and liver after one-week high fat diet intervention with quantitative Raman microscopy

Alexandra Paul^{1,2} | Belén Chanclón³ | Cecilia Brännmark³ |
Pernilla Wittung-Stafshede¹  | Charlotta S. Olofsson³ |
Ingrid Wernstedt Asterholm³ | Sapun H. Parekh^{2,4} 

¹Division of Chemical Biology, Department of Biology and Biological Engineering, Chalmers University of Technology, Gothenburg, Sweden

²Department of Biomedical Engineering, University of Texas at Austin, Austin, Texas, USA

³Department of Physiology (Metabolic Physiology), Institute of Neuroscience and Physiology, Sahlgrenska Academy at the University of Gothenburg, Gothenburg, Sweden

⁴Department of Molecular Spectroscopy, Max Planck Institute for Polymer Research, Mainz, Germany

Correspondence

Sapun H. Parekh, Department of Biomedical Engineering, University of Texas at Austin, 107 W Dean Keeton Street, Austin, TX 78712, USA.
Email: sparekh@utexas.edu

Funding information

Welch Foundation, Grant/Award Number: F-2008-20190330; Svenska Diabetesstiftelsen; Human Frontier Science Program, Grant/Award Number: RGP0045/2018; FP7 People: Marie-Curie Actions, Grant/Award Number: CIG322284; Stiftelserna Wilhelm och Martina Lundgrens; Novo Nordisk Fonden, Grant/Award Number: NNF19OC0056601; Vetenskapsrådet, Grant/Award Numbers: 2013-7107, 2017-00792, 2019-00682, 2020-01463; Kungl. Vetenskaps- och Vitterhets-Samhället i Göteborg; Seventh Framework Programme, Grant/Award Number: 607842

Abstract

Brown adipose tissue (BAT) consists of highly metabolically active adipocytes that catabolize nutrients to produce heat. Playing an active role in triacylglycerol (TAG) clearance, research has shown that dietary fatty acids can modulate the TAG chemistry deposition in BAT after weeks-long dietary intervention, similar to what has been shown in white adipose tissue (WAT). Our objective was to compare the influence of sustained, nonchronic dietary intervention (a 1-week interval) on WAT and interscapular BAT lipid metabolism and deposition in situ. We use quantitative, label-free chemical microscopy to show that 1 week of high fat diet (HFD) intervention results in dramatically larger lipid droplet (LD) growth in BAT (and liver) compared to LD growth in inguinal WAT (IWAT). Moreover, BAT showed lipid remodeling as increased unsaturated TAGs in LDs, resembling the dietary lipid composition, while WAT (and liver) did not show lipid remodeling on this time scale. Concurrently, expression of genes involved in lipid metabolism, particularly desaturases, was reduced in BAT and liver from HFD-fed mice after 1 week. Our data show that BAT lipid chemistry remodels exceptionally

Abbreviations: *Acpat2*, 1-acylglycerol-3-phosphate o-acyltransferase 2; BAT, brown adipose tissue; (B)CARS, broadband coherent anti-Stokes Raman scattering; CD, chow diet; *Cpt1a/b*, carnitine palmitoyltransferase 1A/B; CRM, coherent Raman microscopy; *Dgat1/2*, diacylglycerol o-acyltransferase 1/2; *Elovl6*, elongase; *Fasn*, fatty acid synthase; *Gdp1*, glycerol-3-phosphate dehydrogenase; *Gpam*, glycerol-3-phosphate acyltransferase; HFD, high fat diet; LD, lipid droplet; NEFA, nonesterified fatty acid; *Pck1*, phosphoenolpyruvate carboxykinase 1; *Ppargc1a*, peroxisome proliferator-activated receptor gamma coactivator 1-alpha; *Scd1/2*, stearoyl-CoA desaturase 1/2; SHG, second harmonic generation; *Srebf1c*, sterol regulatory element binding transcription factor 1; TAG, triacylglyceride; TPF, two photon fluorescence; *Ucp1*, uncoupling protein 1.

This is an open access article under the terms of the Creative Commons Attribution License, which permits use, distribution and reproduction in any medium, provided the original work is properly cited.

© 2023 The Authors. *Journal of Cellular Biochemistry* published by Wiley Periodicals LLC.

fast to dietary lipid intervention compared WAT, which further points towards a role in TAG clearance.

KEYWORDS

adipose tissue, diet, mouse, Raman spectroscopy, triacylglycerol

1 | INTRODUCTION

Lipids are efficient energy storage molecules and have evolved in their use as energy repositories to bridge times of energy scarcity. In the developed world, most humans struggle not with food scarcity, but rather, they have essentially unlimited access to nutrients, which has led to a brimming obesity epidemic that is escalating worldwide.¹ A constant positive energy balance (largely resulting from excess nutrient ingestion) leads to increased body weight associated with an increased risk for the development of metabolic diseases such as type 2 diabetes and cardiovascular disease, as well as certain cancers² and increase of the severity of upper respiratory infections.³ Excess energy can be stored as lipids via two distinct pathways: (i) *de novo* lipogenesis from glucose or amino acids or (ii) direct esterification of nonesterified fatty acids (NEFAs). Both pathways will result in formation of neutral lipids, primarily triacylglycerides (TAGs), which are stored in lipid droplets (LDs) located predominantly in adipose tissue.⁴ White adipose tissue (WAT) TAGs derive mostly from direct esterification of NEFAs that are formed either *de novo* in the liver or taken up from the diet.⁵ WAT is also responsible for supplying NEFAs to the other organs to meet the body's energy demand.⁶ Importantly, the balance between uptake and release of NEFAs needs to be tightly controlled, to match the body's energy needs. Excess fatty acids that are stored in the adipose tissue can lead to ectopic lipid deposition associated with chronic inflammation and insulin resistance.^{7,8} Conversely, increased energy expenditure and/or effective storage of excess nutrients in the form of neutral lipids protects against metabolic disturbances.

Searching for possibilities to increase energy expenditure to reduce obesity and its co-morbidities, brown adipose tissue (BAT) has emerged as a potential therapeutic target.^{9–11} BAT is the key site for nonshivering thermogenesis, a process crucial for the ability of small rodents and hibernating animals to keep a constant body core temperature. This heat production is achieved in the mitochondria, which contain uncoupling protein-1 (UCP1) that bypasses the respiratory chain to generate heat instead of ATP from fatty acid oxidation. NEFAs from TAGs are the main fuel for heat production in rodent BAT.¹² Studies of BAT in high fat diet (HFD)-fed rodents showed that BAT mass and lipid content increase during weight gain in mice, indicating that the TAG

accumulation in BAT exceeds the catabolic processes.^{13,14} It was also shown that the TAG chemistry in BAT changes dramatically during cold acclimation and arousal from hibernation, highlighting the plasticity in lipid chemistry in this tissue.¹⁵ Specifically, the amount of unsaturated TAGs in BAT is increased after 72 h of cold exposure demonstrating the importance of lipid chemistry in BAT function.¹⁶ Plasticity in WAT has been observed as the TAG composition in WAT ultimately correlates with the composition of ingested dietary lipids.^{17,18} A similar change in lipid chemistry in BAT can be achieved in mice with 20-week HFD feeding.¹⁹ Interestingly, increased lipid deposition can be observed within the first day of HFD feeding, which shows the acute reaction of BAT to increased lipid intake.²⁰ In humans, increased TAG content in supraclavicular BAT (corresponding to interscapular in rodents) is inversely correlated with insulin sensitivity regardless of body mass index or age.²¹ Further, Aldiss et al.²² found that 72 h of HFD disrupts the peroxisome proliferator-activated receptor signaling an important regulator of lipid metabolism.²³ At the same time, after 72 h HFD the on-set of insulin resistance can be detected and prolonged HFD causes whole body inflammation.²⁴

Other studies have shown that 1 week is sufficient to induce changes in WAT LD size²⁵ and gene expression.²⁶ It is speculated that physiological changes occur rapidly and highly metabolically active tissues like liver bear the initial lipid overload.²⁷ These early changes, the tissue specific roles, and the plasticity of the cellular lipid chemistry is important both for the understanding of insulin resistance, the development of type 2 diabetes, and the potential of BAT as a drug target. Thus, we designed a study using a 1-week HFD intervention to compare the TAG clearing ability of liver, interscapular BAT and WAT, in terms of LD morphology and chemistry. We chose two distinct WAT depots, inguinal (inguinal WAT [IWAT]) and gonadal (gonadal WAT [GWAT]), that have been shown to display distinct hyperplasia/hypertrophy behavior upon HFD.^{28,29} We measure the molecular composition of TAGs and gene expression profiles in BAT, IWAT, gonadal WAT (GWAT, Supporting Information), and liver in mice in response to 1 week of HFD intervention and compare to chow-fed littermates.

Because of the heterogenous cell population in adipose tissue, particularly in BAT,^{30,31} a strong need exists for

microscopy mapping lipid chemistry. Further, recent literature increased the understanding of LDs as highly diverse organelles both inter- and intracellularly.^{32–35} Three different methods are commonly used to study spatially resolved chemical differences: imaging mass spectrometry, electron microscopy, and (coherent) Raman microscopy (CRM). Due to its inherent optical sectioning and relatively simple sample preparation, CRM has recently gained popularity.^{36–40} Here, we used a quantitative CRM method called broadband coherent anti-Stokes Raman Scattering (BCARS) to determine changes in lipid chemistry in liver, BAT, and WAT tissues in response to HFD. Importantly, quantitative BCARS has been validated against the gold-standard of mass spectrometry^{41,42} for quantification of lipid biochemistry (chain length and number of double bonds) and possesses sub-micrometer resolution while requiring virtually no sample preparation. Combining BCARS with additional characterization of lipid metabolism gene expression, we found that HFD diet challenge for as little as 1-week results in differences in lipid uptake/de novo lipogenesis and messenger RNA (mRNA) expression between WAT and BAT (as well as liver) tissues.

2 | MATERIALS AND METHODS

2.1 | Mice and diets

All animal experiments were performed after approval from the local Ethics Committee for Animal Care at the University of Gothenburg, Sweden, and followed appropriate guidelines (2733/20). Male C57BL/6J mice were obtained from Charles River Laboratories at 4 weeks old and allowed to acclimate in the animal facility for 1 week under standard housing conditions with ad libitum access to food and water. For the 1-week intervention, littermates were randomly selected to be either kept on a standard laboratory chow diet (CD; Special Diets Services, $N=5$) or on a HFD (D12492; Research Diets Inc., $N=5$). Mice were fasted for 4 h before tissue collection. Blood glucose levels were measured using a glucometer (Contour from Bayer). Dietary fatty acid composition, mice body weight, and blood glucose levels at the end point can be found in Figures S1 and S2. Interscapular BAT was carefully extracted avoiding peripheral parts that contain white adipocytes. BAT, IWAT, GWAT, and liver were snap-frozen in liquid nitrogen after extraction.

2.2 | Tissue preparation for microscopy

For combined CARS and SHG microscopy whole tissue (BAT, IWAT, GWAT, or liver) was fixed in cold 4%

paraformaldehyde (PFA) containing 150 mM sucrose at 4°C while the tissues thawed and then mounted between a glass cover slide and cover slip (#1) submerged in phosphate buffered saline. For BCARS analysis frozen adipose tissue (IWAT, GWAT, or BAT) was sliced at -39°C in a MTC cryotome (Slee Medical GmbH) using low profile diamond blades (C.L. Sturkey Inc.) into 20 μm thick slices, while liver was cut at -14°C and slices were 10 μm thick. To keep measurements comparable, the tissue was sliced in plane with cells and a central part of the whole tissue extract was chosen. The tissue slices were directly transferred to chilled glass cover slips, immediately covered with 4% PFA containing 150 mM sucrose in the cryotome chamber, sandwiched with a second cover slip, and placed in a refrigerator at 4°C. Afterwards, all cover slide/slip sandwiches were sealed with nail polish before further analysis, and all imaging was done at room temperature.

2.3 | Coherent anti-stokes Raman scattering, two photon fluorescence (TPF), and second harmonic generation microscopy

Lipids, cellular TPF, and collagen were visualized in intact, thawed tissue pieces using a SP 5 II TCS CARS microscope (Leica) equipped with a pico-second pulsed laser source at 817 and 1064 nm (Pico Emerald, APE). Tight focusing conditions were achieved with a water immersion objective ($L \times 25$, $\text{NA} = 0.95$; Leica) and 2845 cm^{-1} CARS signals for lipids were collected above the sample via a CARS 2000 filter set (Leica), allowing the transmission in the range of 2000–3450 cm^{-1} , in front of a photomultiplier tube. In epi direction, TPF and SHG of collagen were collected through a 390/40 nm bandpass filter (FF01-390/40-25-STR; Semrock) on a photomultiplier tube. Regions of interest were randomly selected from distant tissue sites within the same specimen.

2.4 | LD and cell area determination

Regions of interest in the CARS images of all tissues were manually chosen from z-stacks spanning 50–100 μm in depth to achieve the maximum number of LDs that were bisected in the equatorial plane. Then the intracellular droplets were thresholded using the default method in ImageJ and a watershed algorithm was employed to separate LDs. A secondary region of interest was selected manually to only include areas where LDs were perfectly separated by the water shedding. Then, the ImageJ “particle analysis” function was used to calculate LD area. Between three and 10 images were analyzed per

mouse and tissue. Cell areas for BAT are manually estimated from intrinsic TPF of the cells at high contrast settings ($n = 50$ per condition, Figure S3). The cell area was not analyzed for WAT due to the low cytosolic volume and neither for liver due to the unclear cell borders.

2.5 | Broadband CARS (BCARS) microscopy

The home-built setup with custom software written in LabVIEW (National Instruments) has been described in detail before.⁴³ Briefly, a super continuum Stokes beam was generated via a photonic crystal fiber after a dual-output laser source (Leukos-CARS, Leukos), which also provided a narrow band pump/probe beam ($\lambda = 1064$ nm). The Stokes beam was passed through a short pass filter and Glan-Thompson polarizer producing a bandwidth from 1100 to 1600 nm with a power density of $100 \mu\text{W nm}^{-1}$. It was then combined with the pump/probe beam in the focal plane of an inverted microscope (Eclipse Ti-U; Nikon) via an air immersion objective ($\times 100$, NA 0.85; Zeiss). Raster scanning was achieved with a XYZ piezo stage (Nano-PDQ 375 HS; Mad City Labs). The BCARS signals were collected with a $\times 10$ air immersion objective (NA 0.25; Zeiss) above the sample, where the laser beams were removed with a notch (NF03-532/1064E-25; Semrock) and short-pass filter (FES1000) before the signal was analyzed by a spectrometer (Shamrock 303i; Andor) with a CCD camera (Newport DU902P-BR-DD; Andor). The collected spectra ranged from 900 to 3500 cm^{-1} with a spectral pitch of approximately 4 cm^{-1} . Images were collected with 500 nm step size and 15–20 ms pixel dwell for adipose tissues and 250 nm steps with 100 ms pixel dwell for liver. For all samples a reference spectrum was collected in glass. Two spectral images were collected per mouse and tissue.

2.6 | BCARS data analysis

The imaginary component of the third-order Raman susceptibility from the raw BCARS spectra was extracted with a modified Kramers-Kronig algorithm.⁴⁴ This was followed by error-phase correcting employing an iterative noise-maintaining approach that is model-free via the use of a second-order Savitzky-Golay filter (101 spectral points, 404 cm^{-1}).⁴⁵ The resulting Raman-like spectra were fitted pixel by pixel to generate maps of TAG chain length and saturation as described elsewhere.⁴¹ After the

initial fit, an additional threshold of 12–24 carbons and number of double bonds ($\#C = C$) > -0.1 was applied to ensure a physiological range. On average, less than 1% of pixel were discarded in this step, typically at droplet borders where lipid intensity in the spectra was too low to be fitted accurately. The 3×3 images (101×101 pixel) were then stitched and false color coding was applied to display TAG chain length and $\#C = C$.

2.7 | RNA extraction and quantitative real-time PCR

Total RNA from BAT, IWAT, GWAT, and liver was extracted using the TissueLyser LT (Qiagen) and the RNeasy[®] Lipid Tissue Mini Kit (Qiagen) including an on-column DNase digest (RNase-Free DNase Set; Qiagen) according to manufacturer's instructions. RNA concentration and purity were determined with a NanoDrop Spectrometer. A total of 500 ng RNA per sample were used for complementary DNA (cDNA) preparation (High-Capacity cDNA Reverse Transcription Kit; Applied Biosystems) according to the manufacturer's instructions. Quantitative real-time PCR was performed using Fast SYBR[®] Green Master Mix (Applied Biosystems) and the QuantStudio[™] 7 Flex System. Primer sequences are listed in Table S1. A total of 5 ng cDNA was amplified per sample and all samples were amplified in duplicates under nuclease-free conditions. Conditions were 95°C for 20 s (1 cycle), 95°C for 1 s, 60°C for 20 s, 72°C for 15 s (40 cycles), followed by a melting curve (0.5°C/s) from 60°C to 95°C to confirm one PCR-product. Gene-expression was calculated as relative expression to β actin (*Actb*) via $2^{\Delta\text{CT}}$. Further, the foldchange versus CD-fed littermates was calculated via $2^{-\Delta\Delta\text{CT}}$.

2.8 | Statistical analyses

LD area and $2^{\Delta\text{CT}}$ values were averaged per mouse. To compare average TAG chain lengths and number of double bonds between the two dietary conditions, all chain lengths/number of double bonds from two large-area ($150 \times 150 \mu\text{m}^2$) scans per mouse were averaged. Statistical testing was then performed between the two groups of mice. Then a two-tailed, unpaired Mann-Whitney test was performed comparing each HFD intervention with its respective CD control using GraphPad Prism 6. A $p < 0.05$ was considered significant. All p -values for the gene expression analysis are listed in Table S2. Values are typically represented by their mean with standard deviation (*SD*).

3 | RESULTS

3.1 | Experimental outline

To induce obesity, we fed male C57CL/6J mice⁴⁶ either CD or HFD with 7 or 60% caloric intake from lipids, respectively (Figure S1A). The CD supplied 4 kcal% mixed sugars while the HFD contained 6.8 kcal% sucrose. On average, the diets supplied NEFAs with 17.4 (CD)/17.5 (HFD) carbons and 1.3 (CD)/1.0 (HFD) double bonds per lipid chain (Figure S1B,C). Although there was a slight difference in saturation in the two diets, both contained more average #C=C than the average TAG chains we found in all investigated tissues (detailed below). The HFD intervention lasted 1 week and a significant increase in body weight was observed compared to the CD fed mice with similar circulating glucose levels, as expected for mice with the genetic background⁴⁷ (Figure S2).

3.2 | One week of HFD induced changes in LD morphology and increases TAG unsaturation in BAT

In all tissue samples (BAT, WAT, and liver), LDs were easily identified by their strong signal in label-free CARS vibrational imaging at an energy of 2845 cm^{-1} . This imaging highlights CH_2 groups, which are abundant in lipid acyl chains; we and others have used this methodology extensively in lipid imaging.^{41,43,48,49} The LD and cell morphology were investigated in intact, fixed tissue with minimal sample preparation (no embedding or staining). In BAT, we observed that the area of individual LDs increased almost 16-fold after 1 week of HFD as compared to CD controls (Figure 1A,B; LD area distribution: Figure S4A). LDs from HFD BAT covered on average $377 \pm 56\ \mu\text{m}^2$ (mean \pm SD, CD $22 \pm 4\ \mu\text{m}^2$) in area after 1 week (Figure S4A) and adipocytes in BAT from HFD-fed mice appeared to lose their multilocular LD morphology and shift

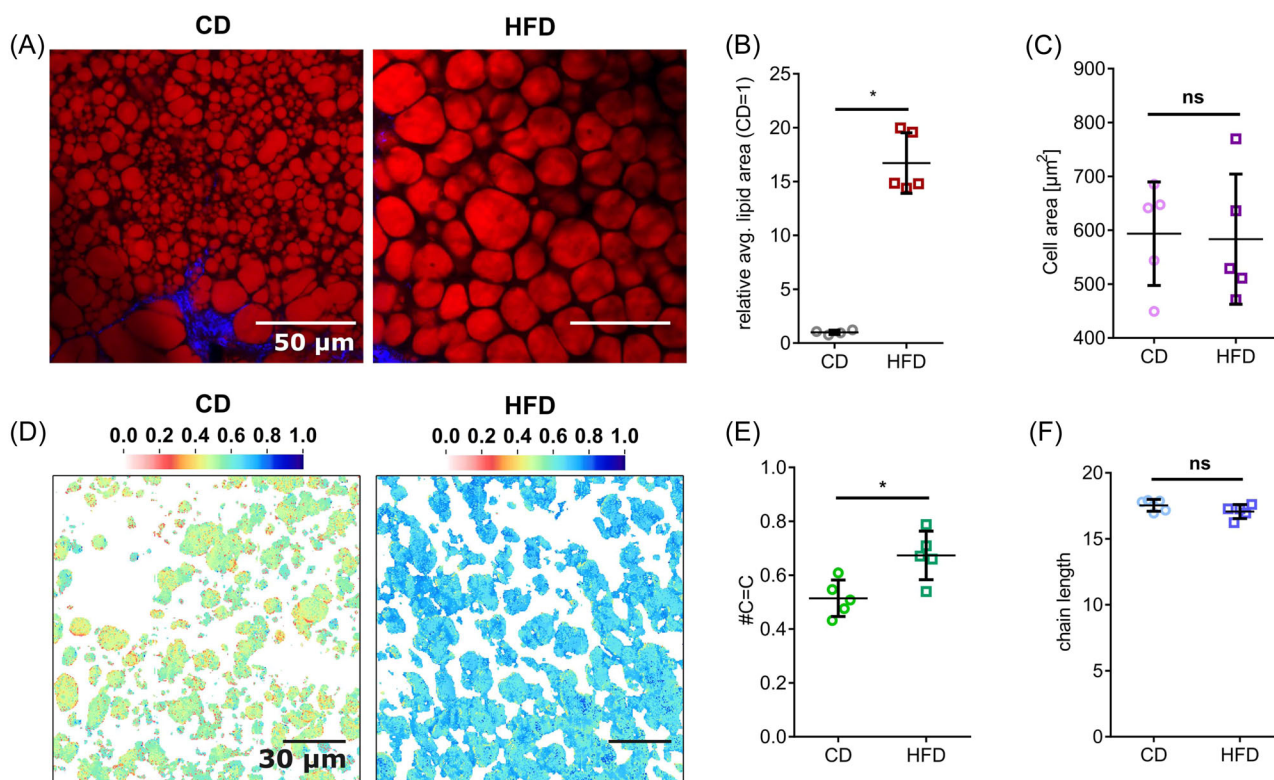


FIGURE 1 HFD-induced changes in BAT. (A) The size of lipid droplets under high fat diet compared to chow diet (red—lipids, single frequency CARS at 2845 cm^{-1} ; blue—SHG, collagen, scale bar: $50\ \mu\text{m}$) increases visibly and quantitatively as seen by the (B), average area per droplet at the equatorial plane in comparison to the chow diet (normalized to 1). Statistical analysis is done between absolute values: $p = 0.0159$. (C) At the same time, the cells in BAT do not increase in size. (D) Images of the average number of double bonds per TAG chain in BAT LDs for CD (left) or after 1-week HFD (right) derived from spectral BCARS scans. (E) Average number of double bonds (all calculated image pixels averaged per mouse) of the TAGs inside the LDs increases significantly after 1 week of HFD feeding in BAT; $p = 0.0079$. (F) Average chain length (all calculated image pixels averaged per mouse) of the TAGs inside the LDs is not affected (as derived from spectral BCARS). Values are displayed as mean \pm SD. * $p < 0.05$ and ** $p < 0.01$ by multiple two-tailed, unpaired Mann–Whitney tests. BAT, brown adipose tissue; BCARS, broadband coherent anti-stokes Raman scattering; CD, chow diet; HFD, high fat diet; LD, lipid droplet.

towards a morphology with 1 large central LD per cell (Figure 1A, top left images), resembling that of white adipocytes. Interestingly, the initial increase of LD area did not lead to an increase in cell size (based on 2-photon autofluorescence) compared to the multilocular CD cells (Figure 1C). Using broadband coherent Raman microscopy (BCARS) on PFA-fixed tissue slices (20 μm for adipose tissue, 10 μm for liver), we analyzed the biochemistry (chain length and number of double bonds) of TAGs in LDs. Our algorithm allows us to map TAG chain length and number of double bonds on a pixel-by-pixel basis.⁴¹ We report the average chain length and unsaturation per fatty acid chain in TAGs over all TAG molecules within a focal volume (300 \times 300 \times 5000 nm). We have previously shown this approach to show absolute accuracy of 0.7 carbons and 0.2 double bonds when compared to GC-MS for more than 10 different oils, with the advantages of mapping TAG chemistry in situ and virtually no sample preparation.⁴¹

From BCARS chemical imaging, we found the number of double bonds—reflecting unsaturation—showed a

significant increase after 1 week of HFD as compared to CD (Figure 1E) and no changes in TAG chain length in the LDs after HFD (Figure 1F). Chemical imaging also showed that the intracellular TAG unsaturation uniformly increased 1 week of HFD feeding (Figure 1D).

3.3 | One-week HFD feeding increased LD area in IWAT and liver while TAG chemistry was unchanged

As in BAT, we mapped the lipid distribution in IWAT using single-frequency CARS microscopy. We found LD hypertrophy after 1 week of HFD in IWAT (~1.7-fold area increase) (Figure 2A,B; LD area distribution: Figure S4B), while the lipid chemistry was not affected (Figure 2C–E). The lipid unsaturation distribution between the 1-week CD and HFD diets are nearly indistinguishable, in contrast to what we found for BAT (Figure 1D).

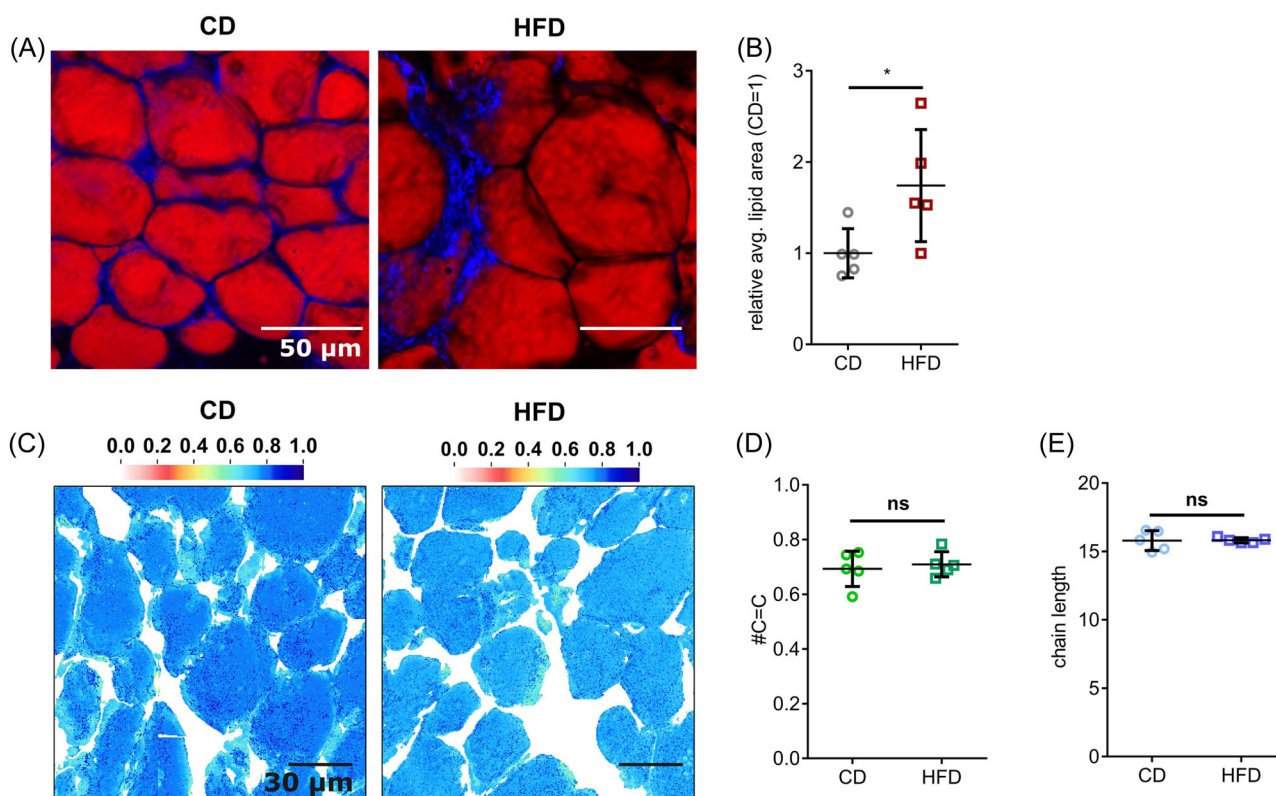


FIGURE 2 HFD-induced changes in IWAT. (A) IWAT shows a less drastic increase in LD size after 1 week of HFD compared to CD (red—lipids, single frequency CARS at 2845 cm^{-1} ; blue—SHG, collagen) as seen by (B), average area per droplet at the equatorial plane (normalized to CD = 1). Statistical analysis is done between absolute values: $p = 0.0317$. (C) Images of the average number of double bonds per TAG chain in IWAT LDs for CD (left) or after 1-week HFD (right) derived from spectral BCARS scans. (D) Average number of double bonds (all calculated image pixels averaged per mouse) per TAG chain is statistically identical under CD or 1 week of HFD feeding. (E) Average lipid chain length (all calculated image pixels averaged per mouse) in TAGs is statistically identical after 1 week of HFD feeding in IWAT (as derived from spectral BCARS). Values are displayed as mean \pm SD. * $p < 0.05$ and ** $p < 0.01$ by multiple two-tailed, unpaired Mann–Whitney tests. BCARS, broadband coherent anti-stokes Raman scattering; CD, chow diet; HFD, high fat diet; IWAT, inguinal white adipose tissue; LD, lipid droplet; TAG, triacylglyceride.

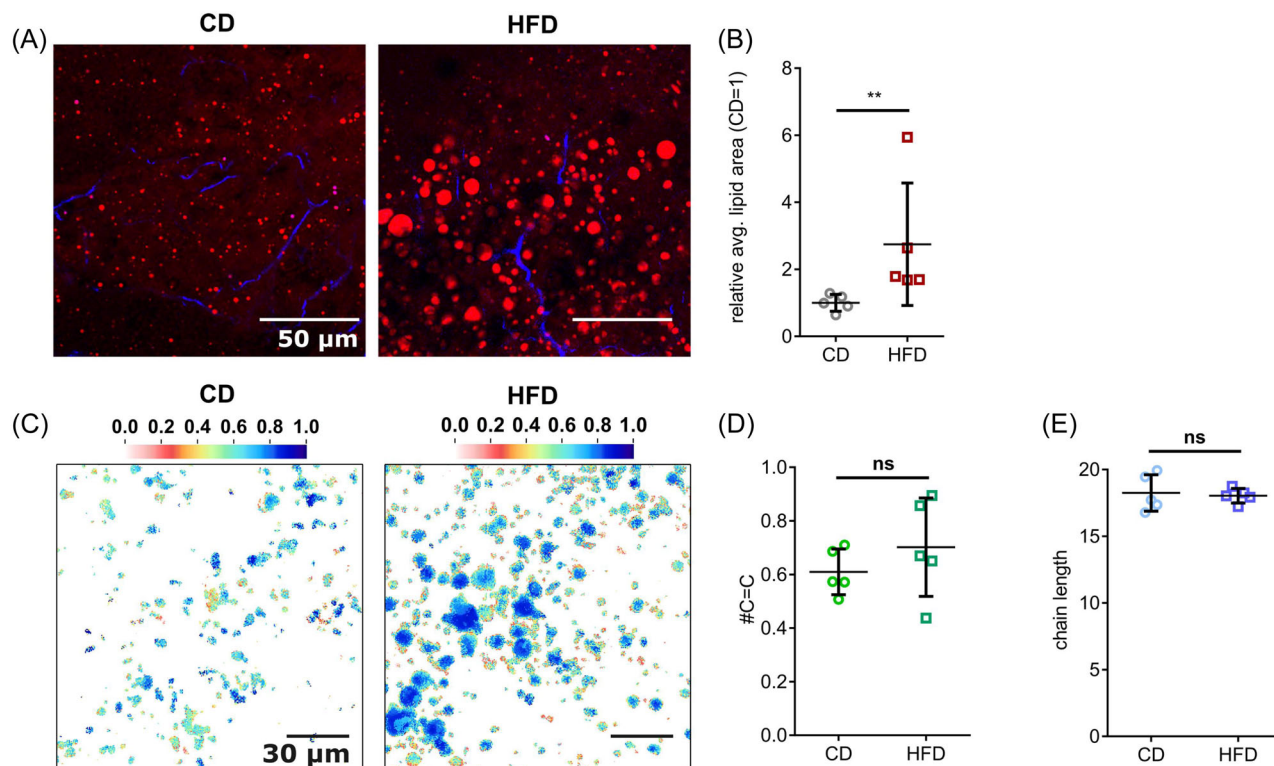


FIGURE 3 HFD induced changes in liver. (A) Liver shows an increase in LD size after 1 week of HFD compared to CD (red—lipids, single frequency CARS at 2845 cm^{-1} ; blue—SHG, collagen) as seen by (B), average area per droplet at the equatorial plane (normalized to $CD = 1$). Statistical analysis is done between absolute values: $p = 0.0079$. (C) Images of the average number of double bonds per TAG chain in liver LDs for CD (left) or after 1-week HFD (right) derived from spectral BCARS scans. (D) Average number of double bonds (all calculated image pixels averaged per mouse) per lipid TAG chain is statistically identical under CD or 1 week of HFD feeding. (E) Average lipid chain length (all calculated image pixels averaged per mouse) in TAGs is statistically identical after 1 week of HFD feeding in liver (as derived from spectral BCARS). Values are displayed as mean \pm SD. * $p < 0.05$ and ** $p < 0.01$ by multiple two-tailed, unpaired Mann–Whitney tests. BCARS, broadband coherent anti-stokes Raman scattering; CD, chow diet; HFD, high fat diet; LD, lipid droplet; TAG, triacylglyceride.

Notably, while all investigated adipose tissues (BAT and WAT) seemed to have stored similar chain lengths (15–17 carbons), the amount of double bonds differed vastly between tissues. Adipocytes in BAT from CD-fed mice contained the lowest abundance of double-bond-containing TAGs (0.53 ± 0.05 , mean \pm SD). In response to 1 week of HFD, TAGs in BAT showed increased double bonds, reaching a level of unsaturation found in IWAT from chow-fed (or HFD) mice ($\#C = C$ bonds in HFD [BAT] = 0.69 ± 0.07 ; $\#C = C$ bonds in CD [IWAT] = 0.68 ± 0.04). This demonstrates a differential remodeling of the BAT versus WAT LDs to the same 1-week dietary intervention. We note that gonadal WAT (GWAT) showed no difference between the two diets in LD size or TAG chemistry (Figure S5). The lower number of double bonds in BAT in mice on the CD highlights the different metabolic state of the two adipose depots.

We next investigated how lipid content and chemistry changed with HFD intervention in the liver since the liver is an important organ in lipid metabolism. Interestingly, we found a drastic (threefold) increase of

LD area in liver after 1 week of HFD (Figure 3A,B; LD area distribution: Figure S4D). As in all BAT tissues, LDs in liver displayed lower # of double bonds compared to the CD in WAT; however, the increase in unsaturation after 1 week on the HFD did not reach statistical significance (Figure 3C,D). The average chain length was not affected by diet (Figure 3E). In comparison to all other investigated tissues, liver LDs showed the highest inter-LD heterogeneity (Figure 3C), particularly for mice on the CD.

3.4 | Genetic changes in BAT, WAT, and liver show reduced de novo lipogenesis

To further probe the mechanism of increased HFD-induced unsaturation in BAT, we compared mRNA expression of numerous genes involved in de novo lipogenesis and lipid modification, particularly fatty acid desaturases (Figure 4A). We found that the expression of genes involved in de novo lipogenesis

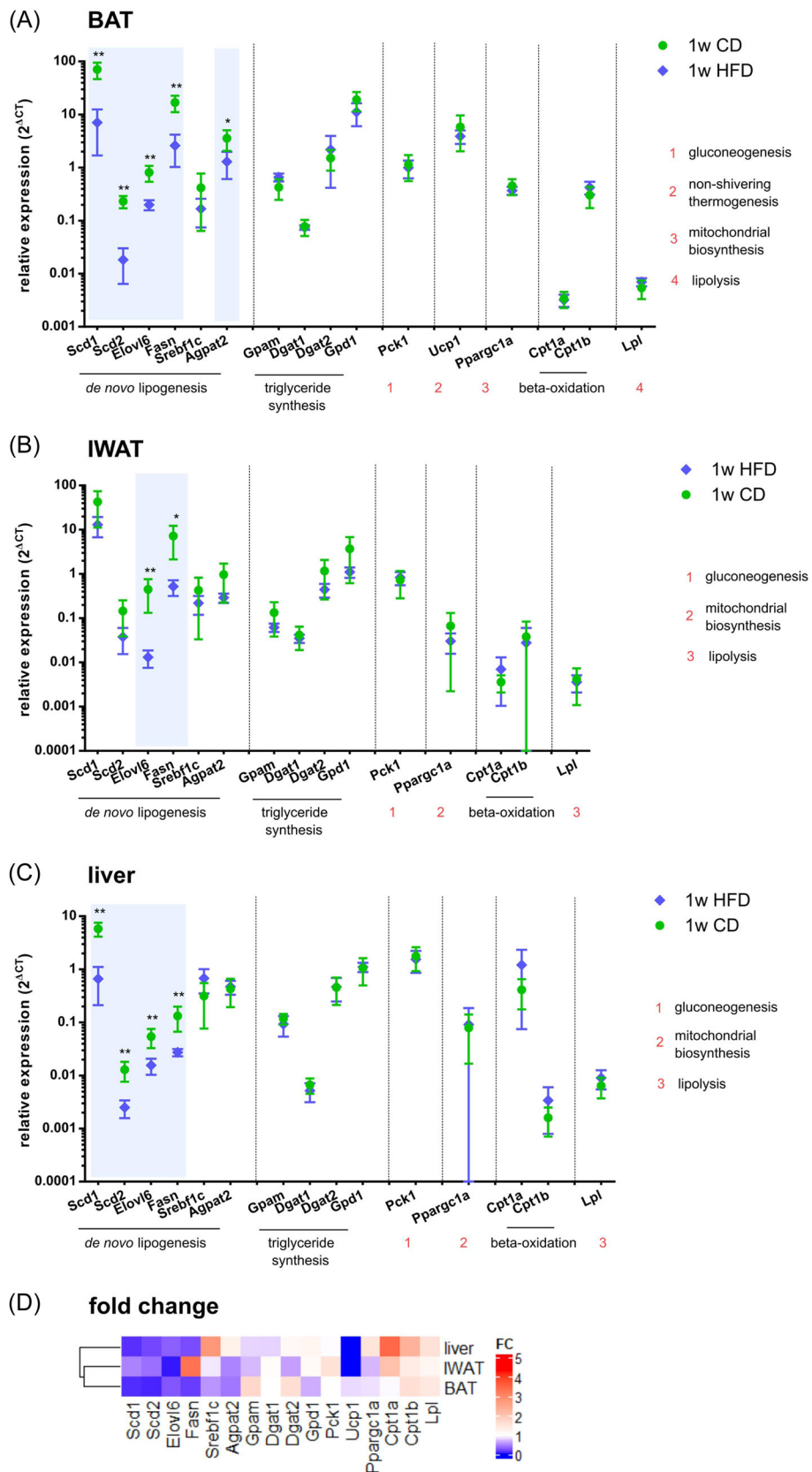


FIGURE 4 Diet induced gene expression changes. Relative gene expression ($2^{-\Delta CT}$) compared to β actin in (A), BAT, (B), IWAT, and (C), liver (green circles—CD, blue diamond—HFD). Significant downregulation in comparison to CD are marked with stars and shaded in blue. All p values can be found in Table S2. $N = 5$. Values are displayed as mean \pm SD. * $p < 0.05$ and ** $p < 0.01$ by multiple two-tailed, unpaired Mann-Whitney tests. (D) Foldchange of gene expression over CD-fed littermates. BAT, brown adipose tissue; BCARS, broadband coherent anti-stokes Raman scattering; CD, chow diet; HFD, high fat diet; IWAT, inguinal white adipose tissue; LD, lipid droplet; TAG, triacylglyceride.

in BAT, e.g., desaturases *Scd1* and *Scd2*, elongase (*Elovl6*) and fatty acid synthase (*Fasn*) was significantly reduced after one week of HFD, as compared to CD. Moreover, *Apat2* (1-acylglycerol-3-phosphate o-acyltransferase 2), an enzyme catalyzing the second step of de novo phospholipid biosynthesis, was also reduced after 1 week of HFD intervention compared to the CD controls. The regulator of sterol biosynthesis, *Srebflc* (sterol regulatory element binding transcription factor 1), was not affected by the HFD. The expression of genes involved in TAG synthesis, *Gpam* (glycerol-3-phosphate acyltransferase, mitochondrial), *Dgat1/2* (diacylglycerol o-acyltransferase 1/2), and *Gpd1* (glycerol-3-phosphate dehydrogenase), was not affected. The expression of *Ucp1* (uncoupling protein 1), related to nonshivering thermogenesis, mitochondrial biosynthesis (*Ppargc1a*—peroxisome proliferator-activated receptor gamma coactivator 1-alpha), *Lpl* (lipoprotein lipase), and gluconeogenesis/glyceroneogenesis (*Pck1*—phosphoenolpyruvate carboxykinase 1) were not significantly different in the HFD mice than in the CD mice. *Cpt1a/b* (carnitine palmitoyltransferase 1B), involved in beta-oxidation, was also unchanged. Taken together, the gene expression analysis suggests that de novo lipogenesis was largely suppressed by HFD intervention even after 1 week, which indicates that the changes in lipid unsaturation in BAT LDs was due to increased dietary NEFA uptake. This is supported by the isotope tracing of lipids in BAT 2 h postfeeding (Figure S7).

In IWAT, mRNA levels of all genes involved in de novo lipogenesis, *Elovl6* and *Fasn*, were reduced after the 1-week HFD intervention (Figure 4B) while all other genes remained unaffected. In GWAT most genes in the de novo lipogenesis pathway were also significantly reduced after 1 week (Figure S6).

Our findings of increased fatty acid content and concurrent downregulation of genes linked to de novo lipogenesis in IWAT and BAT after HFD suggest increased uptake of NEFAs that are then stored as TAGs in those tissues. NEFAs can come from either the diet or liver metabolism, where NEFAs and TAGs are regularly synthesized, signifying the importance of the liver gene expression. Genes involved in the production of longer and more unsaturated chains, *Scd1/2*, *Elovl6*, and *Fasn*, were downregulated after 1-week of HFD analogous to BAT. No other genes were differentially expressed after 1 week (Figure 4C). Once again, it appears that the surplus of available NEFAs from the diet correlates with lower de novo synthesis.

4 | DISCUSSION

In this study, we explored the changes in TAG chemistry in lipid-containing tissues induced by HFD intervention for 1 week. As a complementary approach to studies that rely on radioactive labeling or extraction of all lipids, we investigated both cell and LD morphology and TAG chemistry in intact tissue sections as well as expression of genes involved in various lipid metabolic pathways in the examined tissues. While our lipid quantification method cannot resolve the identity or abundance of individual lipids such as in mass spectrometry, it can accurately map both TAG chain length and #C=C with sub- μm precision unraveling inter- and intracellular differences with almost no sample preparation.

4.1 | HFD induced unilocular LDs in BAT and increases in LD size in all investigated tissues

HFD challenges the whole body with a constant oversupply of lipids that, under isocaloric conditions, would principally be used as energy or stored in WAT depots. However, if the amount of supplied lipids exceeds that which can be stored in WAT, ectopic lipid deposition in nonadipose tissues, like the liver, will occur. It has been shown in humans that not all dietary TAGs in a HFD are metabolized in the liver leading to a “spill-over” to the plasma⁵⁰ from where they can be metabolized by other tissues. These ectopic depositions can arise from long-term lipid-rich diets,⁷ but also as a mechanism to protect the rest of the body during short term overfeeding.^{51,52} Our study focused on a relatively short, sustained intervention (1 week), and we used average LD area to judge the amount of stored lipids in adipose and nonadipose tissues. Our data showed that liver LD area grew significantly, by threefold over CD control, after 1 week (Figure 3B). LD area in BAT showed an even higher increase, 16-fold, after 1 week of HFD. After the HFD dietary intervention, cells in BAT displayed unilocular LDs instead of the multilocular LDs found under CD (Figures 1A and 5). This again implies that BAT is highly responsive to an acute lipid surplus, as has been shown previously.²⁰ The increase in large LDs in BAT after HFD intervention was linked to a “whitening,” coupled to loss of BAT functionality in other studies.⁵³ However, we did not observe any reduction in the mRNA expression of *Ucp1* after HFD intervention, suggesting that BAT still functions in nonshivering thermogenesis. Contrary to BAT and liver, the relative change in IWAT LD area was smaller with no change in GWAT LDs (Figure 2B and Figure S5), highlighting the different response of nominally adipose consumptive versus storage tissues. After

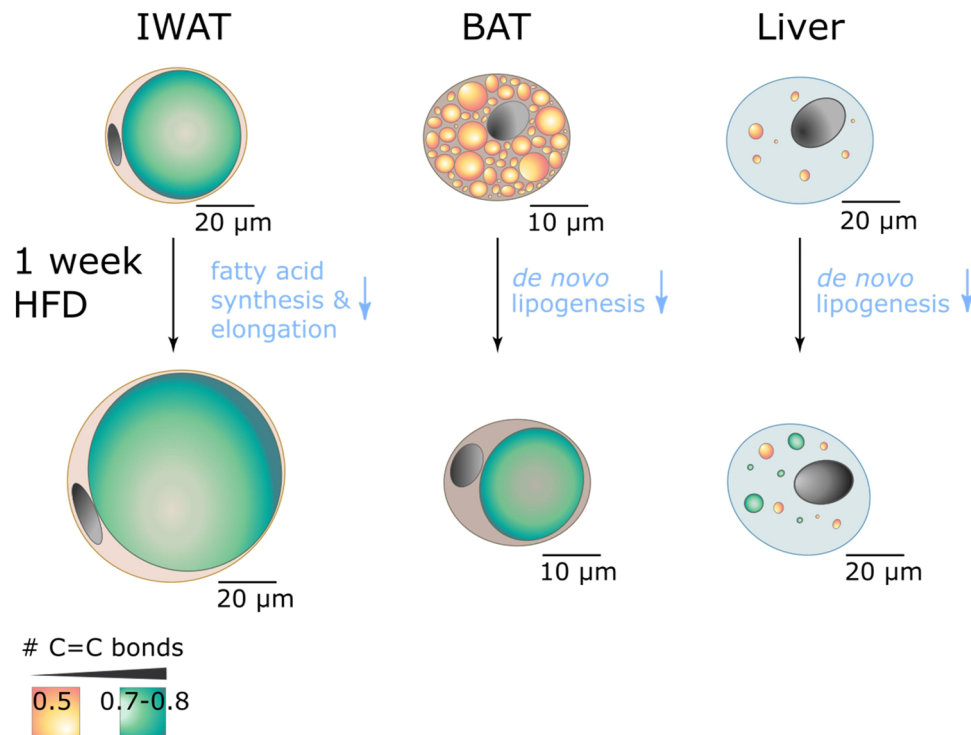


FIGURE 5 Schematic of cellular changes in IWAT, BAT, and liver. The color of the LDs in the cells represents the average number of C = C bonds (orange 0.5 C = C, green 0.7–0.8 C = C). Increases in average LD/cell area are to scale. Pathways where gene expression is reduced are marked in blue. The average LD area is increased in all tissues after 1 week of HFD feeding and adipocytes in BAT display more unilocular LDs. The increase in TAGs correlates with reduced activity in the de novo lipogenesis pathway. However, only BAT shows a uniform significant increase in LD TAG unsaturation. BAT, brown adipose tissue; BCARS, broadband coherent anti-stokes Raman scattering; CD, chow diet; HFD, high fat diet; IWAT, inguinal white adipose tissue; LD, lipid droplet; TAG, triacylglyceride.

4 weeks, all HFD tissues show significant increase in LD size with liver LDs showing the most drastic increase at sixfold compared to their CD-fed littermates (Figure S8A). This suggests that BAT may be the primary protector against lipid overload during short duration high-fat intake whereas WAT may be more important for longer sustained dietary intake of high fat. Additionally, the data after 4-week HFD (Figure S8) indicates that while liver plays a significant role in the metabolism of excess nutritional trigacylglycerol, this effect becomes most pronounced after 4 weeks which further indicates that BAT is the main contributor to early TAG clearance.

4.2 | More unsaturated TAGs are found in LDs during HFD feeding in BAT after 1 week

While HFD increased LD size in all studied tissues, the fatty acids stored as TAGs in BAT showed a marked increase in #C = C bonds. In comparison to the #C = C in extracted tissues (0.43–0.89 as seen using the minimum to maximum values over all tissues from our data), the #

of C = Cs supplied with the diet were 1.0 (HFD). We found that the TAG unsaturation increased with HFD in BAT compared to the CD, a trend that has been observed for BAT after 20 weeks of HFD.¹⁹ After the same intervention of HFD feeding, we found that the TAG chemistry was not significantly affected in IWAT or liver. There are three possible reasons why BAT showed more prominent changes in LD chemistry: (1) reduced de novo lipogenesis and increased uptake of dietary NEFAs, (2) a starting chemical state of TAGs in BAT that was more saturated, or (3) preferential uptake of unsaturated fatty acids in BAT. Our data with isotope labeled triolein, with 1 C = C bond per chain, showed that BAT took up more than fourfold triolein compared to WAT and liver, highlighting a fast clearance of dietary lipids by BAT. This is in line with results reported by Bartelt et al.⁵⁴ describing the rapid clearance of dietary fatty acids by BAT specifically. Combined with the mRNA expression data showing decreased de novo lipogenesis, this supports reason 1. Next, our BCARS data show that TAGs in BAT LD indeed start with fewer C = C bonds, on average, compared to WAT or liver. With a 60% caloric intake on the HFD consisting of unsaturated lipids with

1.0 C=C bond per chain and fast clearance of lipids by BAT, there is “more room” to increase unsaturation in BAT in support of reason 2. Finally, it is also possible that BAT shows preferential uptake of unsaturated dietary fatty acids compared to saturated fatty acids. Previous work has shown that monounsaturated and n-6 polyunsaturated fatty acids were preferably taken up from the diet in the postprandial period for IWAT⁵⁵ in support of reason 3. Therefore, a combination of reasons 1, 2, and 3 could lead to the changes in TAG chemistry in BAT LDs with 1-week HFD.

Turning to WAT, we found no changes in LD unsaturation, suggesting a slower lipid turnover compared to BAT. This is supported by the comparatively low isotope triolein uptake (Figure S7). Our findings on WAT are consistent with that of Brunengraber et al.⁵⁶ that showed incorporation of dietary fatty acids into GWAT in male C57BL/6J mice such that the relative abundance of unsaturated chains (C18:1, C18:2) in the TAGs increased after 34 days compared with 5 days. In liver, TAGs in LDs from the 1-week CD and HFD showed more heterogeneity both in terms of chain length and #C=C bonds compared to WAT or BAT. Such inter-LD heterogeneity in hepatocytes for TAG, cholesterol content, and associated perilipins has been described previously.⁵⁷

4.3 | BAT and liver showed early reduction of genes involved in de novo lipogenesis or lipid chemical modification

In addition to imaging changes in TAG chemistry, we compared mRNA expression of genes involved in modifying TAG chemistry, as well as other genes of interest for TAG storage or utilization. There was a minor difference in sugars supplied by the diets (4% kcal [CD], 6.8% kcal [HFD]), which could potentially drive de novo lipogenesis during HFD. However, we found no differences in *Pck1* (encoding for PEPCK-C the rate-limiting enzyme in gluconeogenesis⁵⁸) in all adipose tissues or liver after HFD compared to CD feeding, suggesting an equal contribution of gluconeogenesis/glyceroneogenesis with both diets. In WAT, uptake of circulating NEFAs from diet or uptake from de novo lipogenesis from the liver is the dominating source of lipids.⁵ Liver is the main contributor to de novo lipogenesis.^{59,60} In all investigated tissues, the fatty acid synthesis pathway (measured by *Fasn* expression) was significantly reduced after 1 week of HFD intervention. This is in line with previous findings that HFD significantly downregulates the contribution of de novo lipogenesis upon 1 week of high-fat feeding in rats.⁶¹

As genetic markers of TAG chemical remodeling, we looked at fatty acid elongase (*Elovl6*) and desaturase enzymes (*Scd1* and *Scd2*), which can modify fatty acid chain length and saturation, respectively. We found *Elovl6* in liver and BAT to be significantly downregulated after 1 week of HFD while the TAG chain lengths were unchanged. HFD-induced downregulation of both *Scd1* and *Scd2* were observed in comparison to CD after 1 week in liver and BAT. If the TAGs inside the LDs would be from de novo lipogenesis, the reduced activity of these key genes would lead to a decrease in desaturation and chain length. However, this trend is not supported by our data on LD chemistry. When the HFD-feeding is extended to 4 weeks, the key genes involved in de novo lipogenesis remain downregulated (Figure S8B). This indicates that the lipid metabolism is enduringly altered and further indicates that these crucial changes occur within the first week of increased nutritional fat supply.

5 | CONCLUSIONS

Our study highlights the different metabolic timescales of BAT, WAT, and liver tissues in response to 1-week HFD challenge. We measured LD size and chemistry in situ in BAT, WAT, and liver isolated from HFD-fed or CD-fed mice using quantitative, label-free chemical microscopy. Connecting these measurements to genetic changes in the same tissues, we found that dietary intervention has distinct effects on BAT and liver compared to WATs. BAT, often considered an oxidative tissue, showed an increase in TAG #C=C and larger increase in LD size in response to HFD intervention after 1 week than WAT, the classical lipid storage tissue. Gene expression analysis supported the notion that dietary fatty acids are suggested to contribute directly to lipid remodeling, with HFD inducing a reduction in expression of genes related to de novo lipogenesis in BAT and liver. Our work suggests that acute uptake of fatty acids is buffered in BAT (and to some extent liver), which not only changes LD size but also composition.

AUTHOR CONTRIBUTIONS

Alexandra Paul, Ingrid Wernstedt Asterholm, Sapun H. Parekh: conceptualized the study. **Alexandra Paul, Belén Chanclón, Cecilia Brännmark:** performed the experiments and data analysis. **Pernilla Wittung-Stafshede, Charlotta S. Olofsson, Ingrid Wernstedt Asterholm, Sapun H. Parekh:** contributed materials and scientific discussion. **Alexandra Paul, Sapun H. Parekh:** drafted the manuscript and all authors contributed edits.

ACKNOWLEDGMENTS

We thank Frederik F. Fleissner for support with the BCARS setup. The research leading to these results has received funding from the European Union's Seventh Framework Program (FP7/2007-2013) under grant agreement no. 607842, Kungl. Vetenskaps-och Vitterhets-Samhället, Wilhem och Martina Lundgrens Stiftelse, Marie Curie Foundation no. CIG322284, Swedish Research Council (2013-7107, 2017-00792, 2019-00682, and 2020-01463), Novo Nordisk Foundation (NNF19OC0056601), Swedish Diabetes Foundation, Welch Foundation (F-2008-20190330 and F-2008-20220331), and the Human Frontiers in Science Program (RGP0045/2018). Open Access funding enabled and organized by Projekt DEAL.

CONFLICTS OF INTEREST

The authors declare no conflicts of interest.

DATA AVAILABILITY STATEMENT

Data that support the findings of this study are provided in the article and its Supplementary Information. All data available from the authors on request.

ORCID

Pernilla Wittung-Stafshede  <http://orcid.org/0000-0003-1058-1964>

Sapun H. Parekh  <http://orcid.org/0000-0001-8522-1854>

REFERENCES

1. Jaacks LM, Vandevijvere S, Pan A, et al. The obesity transition: stages of the global epidemic. *Lancet Diabetes Endocrinol.* 2019;7:231-240.
2. Nawrocki AR, Scherer PE. Keynote review: the adipocyte as a drug discovery target. *Drug Discovery Today.* 2005;10:1219-1230.
3. Gao F, Zheng KI, Wang X-B, et al. Obesity is a risk factor for greater COVID-19 severity. *Diabetes Care.* 2020;43:e72-e74.
4. Scherer PE. Adipose tissue. *Diabetes.* 2006;55:1537-1545.
5. Strawford A, Antelo F, Christiansen M, Hellerstein MK. Adipose tissue triglyceride turnover, de novo lipogenesis, and cell proliferation in humans measured with ²H₂O. *Am J Physiol.* 2004;286:E577-E588.
6. Nye C, Kim J, Kalhan SC, Hanson RW. Reassessing triglyceride synthesis in adipose tissue. *Trends Endocrinol Metab.* 2008;19:356-361.
7. Unger RH, Scherer PE. Gluttony, sloth and the metabolic syndrome: a roadmap to lipotoxicity. *Trends Endocrinol Metab.* 2010;21:345-352.
8. Borén J, Taskinen M-R, Olofsson S-O, Levin M. Ectopic lipid storage and insulin resistance: a harmful relationship. *J Intern Med.* 2013;274:25-40.
9. Harms M, Seale P. Brown and beige fat: development, function and therapeutic potential. *Nature Med.* 2013;19:1252-1263.
10. Frühbeck G, Becerril S, Sáinz N, Garrastachu P, Garcia-Velloso MJ. BAT: a new target for human obesity? *Trends Pharmacol Sci.* 2009;30:387-396.
11. Candelore MR, Deng L, Tota LM, Kelly LJ, Cascieri MA, Strader CD. Pharmacological characterization of a recently described human beta 3-adrenergic receptor mutant. *Endocrinology.* 1996;137:2638-2641.
12. Cannon B, Nedergaard J. Brown adipose tissue: function and physiological significance. *Physiol Rev.* 2004;84:277-359.
13. Clerte M, Baron DM, Brouckaert P, et al. Brown adipose tissue blood flow and mass in obesity: a contrast ultrasound study in mice. *J Am Soc Echocardiogr.* 2013;26:1465-1473.
14. Kuipers EN, Kantae V, Maarse BCE, et al. High fat diet increases circulating endocannabinoids accompanied by increased synthesis enzymes in adipose tissue. *Front Physiol.* 2019;9:1913. doi:10.3389/fphys.2018.01913
15. Carneheim C, Cannon B, Nedergaard J. Rare fatty acids in brown fat are substrates for thermogenesis during arousal from hibernation. *Am J Physiol.* 1989;256:R146-R154.
16. Marcher A-B, Loft A, Nielsen R, et al. RNA-Seq and mass-spectrometry-based lipidomics reveal extensive changes of glycerolipid pathways in brown adipose tissue in response to cold. *Cell Rep.* 2015;13:2000-2013.
17. Field CJ, Angel A, Clandinin MT. Relationship of diet to the fatty acid composition of human adipose tissue structural and stored lipids. *Am J Clin Nutr.* 1985;42:1206-1220.
18. Body DR. The lipid composition of adipose tissue. *Prog Lipid Res.* 1988;27:39-60.
19. Grzybek M, Palladini A, Alexaki VI, et al. Comprehensive and quantitative analysis of white and brown adipose tissue by shotgun lipidomics. *Mol Metab.* 2019;22:12-20.
20. Kuipers EN, Held NM, in het Panhuis W, et al. A single day of high-fat diet feeding induces lipid accumulation and insulin resistance in brown adipose tissue in mice. *Am J Physiol Endocrinol Metab.* 2019;317:E820-E830.
21. Raiko J, Holstila M, Virtanen KA, et al. Brown adipose tissue triglyceride content is associated with decreased insulin sensitivity, independently of age and obesity. *Diabetes, Obes Metab.* 2015;17:516-519.
22. Aldiss P, Lewis JE, Boocock DJ, et al. Interscapular and perivascular brown adipose tissue respond differently to a short-term high-fat diet. *Nutrients.* 2019;11:1065.
23. Ahmadian M, Suh JM, Hah, N, et al. PPAR γ signaling and metabolism: the good, the bad and the future | Nature Medicine. *Nat. Med.* 19, 2013:557-566.
24. Lee YS, Li P, Huh JY, et al. Inflammation is necessary for long-term but not short-term high-fat diet-induced insulin resistance. *Diabetes.* 2011;60:2474-2483.
25. Jo J, Gavrilova O, Pack S, et al. Hypertrophy and/or hyperplasia: dynamics of adipose tissue growth. *PLoS Comput Biol.* 2009;5:e1000324.
26. Gao M, Ma Y, Liu D. High-fat diet-induced adiposity, adipose inflammation, hepatic steatosis and hyperinsulinemia in outbred CD-1 mice. *PLoS One.* 2015;10:e0119784.
27. Kleemann R, van Erk M, Verschuren L, et al. Time-resolved and tissue-specific systems analysis of the pathogenesis of insulin resistance. *PLoS One.* 2010;5:e8817.

28. von Frankenberg AD, Marina A, Song X, Callahan HS, Kratz M, Utschneider KM. A high-fat, high-saturated fat diet decreases insulin sensitivity without changing intra-abdominal fat in weight-stable overweight and obese adults. *Eur J Nutr*. 2017;56:431-443.
29. van Beek L, van Klinken JB, Pronk ACM, et al. The limited storage capacity of gonadal adipose tissue directs the development of metabolic disorders in male C57Bl/6J mice. *Diabetologia*. 2015;58:1601-1609.
30. Lynes MD, Tseng Y-H. Deciphering adipose tissue heterogeneity: adipose tissue heterogeneity. *Ann NY Acad Sci*. 2018;1411:5-20.
31. Sun W, Modica S, Dong H, Wolfrum C. Plasticity and heterogeneity of thermogenic adipose tissue. *Nature Metabolism*. 2021;3:751-761.
32. Pacia MZ, Sternak M, Mateuszuk L, Stojak M, Kaczor A, Chlopicki S. Heterogeneity of chemical composition of lipid droplets in endothelial inflammation and apoptosis. *Biochim Biophys Acta Mol Cell Res*. 2020;1867:118681.
33. Herms A, Bosch M, Ariotti N, et al. Cell-to-cell heterogeneity in lipid droplets suggests a mechanism to reduce lipotoxicity. *Curr Biol*. 2013;23:1489-1496.
34. Zhang S, Wang Y, Cui L, et al. Morphologically and functionally distinct lipid droplet subpopulations. *Sci Rep*. 2016;6:29539.
35. Alamri H, Patterson NH, Yang E, et al. Mapping the triglyceride distribution in NAFLD human liver by MALDI imaging mass spectrometry reveals molecular differences in micro and macro steatosis. *Anal Bioanal Chem*. 2019;411:885-894.
36. Nahmad-Rohen A, Regan D, Masia F, et al. Quantitative label-free imaging of lipid domains in single bilayers by hyperspectral coherent Raman scattering. *Anal Chem*. 2020;92:14657-14666.
37. Chen W-W, Lemieux GA, Camp CH, Chang T-C, Ashrafi K, Cicerone MT. Spectroscopic coherent Raman imaging of *Caenorhabditis elegans* reveals lipid particle diversity. *Nat Chem Biol*. 2020;16:1087-1095.
38. Xu J, Yu T, Zois CE, et al. Unveiling cancer metabolism through spontaneous and coherent Raman spectroscopy and stable isotope probing. *Cancers*. 2021;13:1718.
39. Flynn JD, Gimmen MY, Dean DN, Lacy SM, Lee JC. Terminal alkynes as Raman probes of α -Synuclein in solution and in cells. *ChemBioChem*. 2020;21:1582-1586.
40. Chiu Y-F, Huang C-K, Shigeto S. In vivo probing of the temperature responses of intracellular biomolecules in yeast cells by label-free Raman microspectroscopy. *ChemBioChem*. 2013;14:1001-1005.
41. Paul A, Wang Y, Brännmark C, Kumar S, Bonn M, Parekh SH. Quantitative mapping of triacylglycerol chain length and saturation using broadband CARS microscopy. *Biophys J*. 2019;116:2346-2355. doi:10.1016/j.bpj.2019.04.036
42. Daemen S, Gemmink A, Paul A, et al. Label-free CARS microscopy reveals similar triacylglycerol acyl chain length and saturation in myocellular lipid droplets of athletes and individuals with type 2 diabetes. *Diabetologia*. 2020;63:2654-2664.
43. Billecke N, Rago G, Bosma M, et al. Chemical imaging of lipid droplets in muscle tissues using hyperspectral coherent Raman microscopy. *Histochem Cell Biol*. 2014;141:263-273.
44. Liu Y, Lee YJ, Cicerone MT. Fast extraction of resonant vibrational response from CARS spectra with arbitrary nonresonant background. *J Raman Spectrosc*. 2009;40:726-731.
45. Zhao J, Lui H, Mclean DI, Zeng H. Automated autofluorescence background subtraction algorithm for biomedical Raman spectroscopy. *Appl Spectrosc*. 2007;61:1225-1232.
46. Wang C, Liao JK. A mouse model of diet-induced obesity and insulin resistance. *Methods Mol Biol*. 2012;821:421-433.
47. Winzell M, Ahrén B. The high-fat diet-fed mouse. *Diabetes*. 2004;53:S215-S219.
48. Evans CL, Xie XS. Coherent anti-stokes Raman scattering microscopy: chemical imaging for biology and medicine. *Annu Rev Anal Chem*. 2008;1:883-909.
49. Daemen S, van Zandvoort MAMJ, Parekh SH, Hesselink MKC. Microscopy tools for the investigation of intracellular lipid storage and dynamics. *Mol Metab*. 2016;5:153-163.
50. Fielding B. Tracing the fate of dietary fatty acids: metabolic studies of postprandial lipaemia in human subjects. *Proc Nutr Soc*. 2011;70:342-350.
51. Gauthier M-S, Favier R, Lavoie J-M. Time course of the development of non-alcoholic hepatic steatosis in response to high-fat diet-induced obesity in rats. *Br J Nutr*. 2006;95:273-281.
52. Asterholm IW, Scherer PE. Enhanced metabolic flexibility associated with elevated adiponectin levels. *Am J Pathol*. 2010;176:1364-1376.
53. Shimizu I, Arahamian T, Kikuchi R, et al. Vascular rarefaction mediates whitening of brown fat in obesity. *J Clin Invest*. 2014;124:2099-2112.
54. Bartelt A, Bruns OT, Reimer R, et al. Brown adipose tissue activity controls triglyceride clearance. *Nature Med*. 2011;17:200-205.
55. Summers LK, Barnes SC, Fielding BA, et al. Uptake of individual fatty acids into adipose tissue in relation to their presence in the diet. *Am J Clin Nutr*. 2000;71:1470-1477.
56. Brunengraber DZ, McCabe BJ, Kasumov T, Alexander JC, Chandramouli V, Previs SF. Influence of diet on the modeling of adipose tissue triglycerides during growth. *Am J Physiol Endocrinol Metab*. 2003;285:E917-E925.
57. Hsieh K, Lee YK, Londos C, Raaka BM, Dalen KT, Kimmel AR. Perilipin family members preferentially sequester to either triacylglycerol-specific or cholesteryl-ester-specific intracellular lipid storage droplets. *J Cell Sci*. 2012;125:4067-4076.
58. Beale E, Hammer R, Antoine B, Forest C. Disregulated glyceroneogenesis: PCK1 as a candidate diabetes and obesity gene. *Trends Endocrinol Metab*. 2004;15:129-135.
59. Sjöström L. Fatty acid synthesis de novo in adipose tissue from obese subjects on a hypercaloric high-carbohydrate diet. *Scand J Clin Lab Invest*. 1973;32:339-349.
60. Björntorp P, Sjöström L. Carbohydrate storage in man: speculations and some quantitative considerations. *Metabolism*. 1978;27:1853-1865.

61. Delgado TC, Pinheiro D, Caldeira M, et al. Sources of hepatic triglyceride accumulation during high-fat feeding in the healthy rat. *NBM*. 2009;22:310-317.

SUPPORTING INFORMATION

Additional supporting information can be found online in the Supporting Information section at the end of this article.

How to cite this article: Paul A, Chanclón B, Brännmark C, et al. Comparing lipid remodeling of brown adipose tissue, white adipose tissue, and liver after one-week high fat diet intervention with quantitative Raman microscopy. *J Cell Biochem*. 2023;124:382-395. doi:10.1002/jcb.30372